Unveiling the electron-induced ionization cross-sections and fragmentation mechanisms of 3,4-dihydro-2H-pyran

Tomasz J. Wasowicz[1,2*], Michal K. Jurkowski[2], Allison L. Harris[3], Ivan Ljubić[4]

[1]BioTechMed Center, Gdańsk University of Technology, ul. Narutowicza 11/12, 80-233 Gdańsk, Poland

[2]Division of Complex Systems Spectroscopy, Institute of Physics and Applied Computer Science, Faculty of Applied Physics and Mathematics, Gdansk University of Technology, ul. G. Narutowicza 11/122, 80-233 Gdańsk, Poland

[3]Physics Department, Illinois State University, Normal, IL 61790, USA

[4]Department of Physical Chemistry, Ruđer Bošković Institute, Bijenička cesta 54, HR-10000 Zagreb, Croatia

*E-mail: tomasz.wasowicz1@pg.edu.pl

TJW: http://orcid.org/0000-0001-5179-4021

MKJ: https://orcid.org/0000-0002-0576-7687

AH: https://orcid.org/0000-0003-2689-982X

IL: https://orcid.org/0000-0002-3395-7293

Keywords: Cancer, collision, electron, ionization, fragmentation, cross-section, 3,4-dihydro-2H-pyran, molecular dynamics, QCxMS formalism, machine learning simulations

Abstract

The interactions of electrons with molecular systems under various conditions are essential to interdisciplinary research fields extending over the fundamental and applied sciences. In particular, investigating electron-induced ionization and dissociation of molecules may shed

light on the radiation damage to living cells, the physicochemical processes in interstellar environments, and reaction mechanisms occurring in combustion or plasma. We have therefore studied electron-induced ionization and dissociation of the gas phase 3,4-dihydro-2H-pyran (DHP), a cyclic ether appearing to be a viable moiety for developing efficient clinical pharmacokinetics and revealing the mechanisms of biofuel combustion. The mass spectra in the m/z = 10–90 mass range were measured at several different energies of the ionizing electron beam using mass spectrometry. The mass spectra of DHP at the same energies were simulated using on-the-fly semi-classical molecular dynamics (MD) within the framework of the QCxMS formalism. The MD settings were suitably adjusted until a good agreement with the experimental mass spectra intensities was achieved, thus enabling a reliable assignment of cations and unraveling the plausible fragmentation channels. Based on the measurement of the absolute total ionization cross-section of DHP $(18.1\pm0.9)\times10^{-16}$ cm^2 at 100 eV energy, the absolute total and partial ionization cross-sections of DHP were determined in the 5–140 eV electron energy. Moreover, a machine learning algorithm that was trained with measured cross-sections from 25 different molecules was used to predict the total ionization cross-section for DHP. Comparison of the machine learning simulation with the measured data showed acceptable agreement, similar to that achieved in past predictions of the algorithm.

1. Introduction

Apart from the positive impact on the natural human environment, the development of civilization has brought many unfavorable changes over the past few decades. The biological effects of chemization, environmental pollution, and the growing problem of obesity (caused by decreased physical activity, processed foods, disruptors, stress, and

depression) lead to spontaneous gene mutations and the growth of various cancers [1], [2]. The emergence of these factors, in turn, stimulates the development of medical methods. For instance, significant advances in cancer therapies are being made in treatment approaches employing different kinds of ionizing radiation (see, e.g., [3]-[6]). Radiation may directly affect the cancerous cells at the molecular level, producing physical and chemical alterations by excitations, ionizations, and bond cleavages in the DNA helix and surrounding medium (DNA itself, water, and other nearby biomolecules) [7]. These modifications result mainly from the interactions of the primary ionizing beams [7], [8]. However, the impact of secondary particles, such as low-energy electrons, radicals, and ions, generated along the incident track of the radiation [7], [8] cannot be neglected. In particular, the secondary free electrons are responsible for initiating the processes relevant to the breakage of single and double strands of DNA helix [4], [9], [10], [11]. Therefore, the interactions of electrons (e.g., [10]-[18]), photons (e.g., [19]-[28]), radicals [29], and ions (e.g., [30]-[41]) with the backbone molecules of the DNA helix (deoxyribose sugar, nitrogen bases) and their analogs (such as tetrahydrofuran, furan, isoxazole, pyrimidine, pyridine, pyrrole, etc.) have been extensively investigated.

The mechanisms of radiation-induced damage to these molecules are complex and have not yet been fully elucidated. The interdisciplinary surveys encompassing different complexity levels, from the study of isolated gas-phase DNA building blocks to whole cells and even organisms, are being used to unravel these mechanisms. The gas-phase investigations provide information on the direct processes taking place at the lowest level of complexity of the collisional system without the presence of a chemical environment. In contrast, interactions closer to those occurring in the natural cell environment can be studied in the liquid phase or using thin films.

Depending on the type of cancer, patients may undergo additional treatment, including targeted therapy, which uses molecularly targeted drugs to hinder the growth and spread of specific cancer cells [42]. Combining radio- or hadron-therapy with proper drug treatment can additionally inhibit the proliferation of cancer cells with less damage to healthy cells and thus significantly improve survival rates [43]. This is because these pharmaceuticals are molecularly targeted to tumor cells, making them more sensitive to radiation [43]. In addition, the direct interaction of radiation on the accumulated drugs can lead to their fragmentation, increasing the number of reactive species that interact with the adjacent medium [43]. However, such anti-cancer therapy necessitates new oxygen-enriched pharmaceutical compounds [44]. Accordingly, various radiosensitizers have been developed to increase the effectiveness of radiotherapy itself; see, for example, [45] and references therein. Nevertheless, the medicaments synthesized from dihydropyran derivatives better meet the requirements of combined targeted therapies. Indeed, anthracyclines, a class of drugs built on dihydropyran ring, are broad-spectrum antitumor agents that induce, among other things, indirect damage to DNA via reactions involving reactive oxygen species and are not as toxic as many other radiosensitizers [46].

Dihydropyran is a heterocyclic unsaturated oxine with the formula C_5H_8O. It consists of two isomeric forms that differ by the location of the double bond. The 3,4-dihydro-2H-pyran (DHP) ring (Figure 1) has an unsaturation adjacent to oxygen. The isomeric 3,6-dihydro-2H-pyran has a methylene moiety incorporated between the oxygen and double bond.

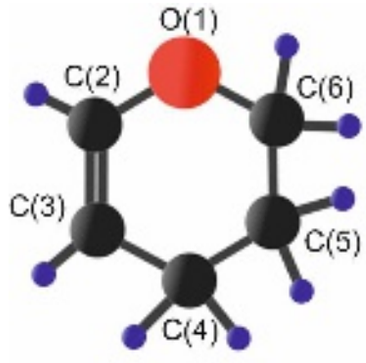

Figure 1. The DHP molecule, C_5H_8O, showing the labeling of the atoms. Color code: The carbon atom is gray, the oxygen atom is red, and the hydrogen atom is blue.

Although the dihydropyran ring exemplifies a promising scaffold in synthesizing new medicines [46]-[49] as well as being incorporated into naturally occurring substances (e.g., green tea catechins [50]) and compounds of importance to the combustion chemistry of oxygenated biofuels [51], very little is known about its interaction with different types of radiation. Besides the electron-induced mass spectrometric investigation deciphering primary reaction mechanisms in 29 cyclic ethers important in low-temperature combustion performed by Koritzke et al. [52], measurements of fragmentation of DHP by electron impact are non-existent. In the mentioned study [52], the mass spectrum of DHP was only measured at 70 eV, and the processes leading to the formation of the most intensive m/z = 55 and 39 peaks were suggested. Furthermore, on the basis of experimental data on the fragmentation of these ethers, especially oxanes, combined with an analysis of various theoretical models, Koritzke et al. [52] proposed oxygen O(1) as the site most susceptible to electron removal. It was also suggested that the carbon site C(3) is prone to ionization. The parent cations of DHP may then undergo two major decomposition pathways. A transannular cleavage of O(1)–C(6) and C(2)=C(3) occurring across the DHP ring in a single

step may lead to the production of the m/z = 55 fragment. The second pathway may start from inductive cleavage (initiated from the charge site), followed by the open ring structure rearrangement, and the allene (corresponding to the m/z = 39 cation) detachment via the radical-site initiated fragmentation (i.e., α-cleavage).

In the present work, the electron-induced dissociative ionization of the isomeric 3,4-dihydro-2H-pyran molecule has been experimentally and theoretically investigated for the first time. In particular, we have recorded the mass spectra in the m/z = 10–90 mass range for several electron energies using a quadrupole mass spectrometer. Then, we used theoretical molecular dynamics calculations to identify and interpret the observed spectral features and unravel possible fragmentation mechanisms. We have also determined the total and partial ionization cross-sections (σ) of 41 cations in the energy range from their respective appearance energies (E_{TH}) to 140 eV. To complete the above results, we have performed machine learning simulations predicting total ionization cross-sections.

2. Experimental Method

The experiment was performed using electron impact mass spectrometry (EIMS) at the Laboratory of Complex Systems Spectroscopy (Fahrenheit Universities' core lab) of the Gdansk University of Technology. The apparatus and measuring methodology were presented earlier (e.g., [53], [54]). Thus, only a summary connected with DHP details is given here. A more detailed description of experimental procedures and conditions is presented in the supplementary material.

Briefly, the EPIC 300 (Hiden Analytical Ltd.) mass spectrometer involved an internal electron gun as the ionization source, the ion extractor, focusing electrodes, and energy filter electrodes installed in front of the quadrupole mass filter. The ionization region was

surrounded by the cage with positive voltages. It allowed extracting electrons from the source. The extracted electrons were formed in the beam via focusing electrodes. The electron beam current was usually 0.3 or 30 μA. Then, the incident electron beam collided with the effusive beam of 3,4-dihydro-2H-pyran delivered into the collision region by a narrow stainless steel capillary. During the collisions, the DHP target was ionized and decomposed. The charged products were extracted from the colliding region by an electrode at −200 V potential directed through the mass filter to the ion detector mounted at the end of the quadrupole electrodes. The extraction efficiency of the spectrometer was checked to be reasonably constant in the mass region from about m/z = 10-120 as deduced from measurements of the mass spectra in CO_2 [53] and CCl_4 [55]. From the retardation curves measured by increasing the positive voltage of the filter electrode, the initial kinetic energies of the fragment cations were estimated. The analysis performed for several different molecules showed that lighter cations (such as m/z = 26) had an energy of not more than 0.5 eV, whereas heavier cationic species (such as m/z = 55) had an energy much less than 0.5 eV. The mass resolution of the spectrometer was derived from the measured spectra to be about one Dalton (u).

The spectrometer operated in two regimes. In the first regime, the mass spectra were collected in the m/z = 10–90 mass range at the fixed electron beam energies. In the second one, the spectrometer was set up on a particular mass peak, and its intensity was measured at the 5-140 eV energy range. These measurements were performed with the 1 eV energy steps. As a result, the cation yield curves were obtained. The appearance energies of the cation fragments were then obtained from their cation yield curves measured in narrow energy regions around the expected positions of these thresholds. In these determinations, the energy steps were typically much smaller than 1 eV. Each cation yield curve was

determined several times for different pressures, currents, and recording times. The energy scale was calibrated in relation to the known Ar^+ ionization threshold (15.759±0.001 eV [56]) with an accuracy of ±0.015 eV. In addition, the energy dispersion distribution of the electron beam was estimated to be 600 meV from the Ar^+ yield measured just above its appearance energy.

The base pressure in the spectrometer's vacuum chamber was kept at 10^{-8} mbar. The vacuum was achieved using a 70 l/sec turbomolecular pump. The operating pressure with DHP vapors in the collision cell was set at $1–3\times10^{-6}$ mbar. However, during cross-section determinations, we extended the pressure range from 5.7×10^{-7} mbar to 4.2×10^{-6} mbar. Throughout the measurements, care was taken to maintain linear dependence between the detected cation signal and the target gas pressure. The cation signal was linear as a function of the DHP gas pressure up to 6×10^{-6} mbar. Preserving the state of linearity between these parameters is very important because it indicates the conditions of a single collision regime.

The liquid 3,4-dihydro-2H-pyran had a purity of 97% and was procured from Sigma Aldrich, Poland [57]. At the beginning of the experiment, the DHP sample was degassed several times in a stainless steel container under a vacuum to remove residual vapors. The measurements were performed at room temperature because of the high enough vapor pressure of DHP, ca. 74.4±0.1 mmHg at 25 °C [58]. However, the whole spectrometer (particularly the vacuum chamber and valves) was slightly heated to avoid DHP condensation. Special care was taken to maintain the highest possible purity of each piece of equipment (for more information, see supplementary material). Moreover, special care was taken to ensure that the apparatus was completely sealed. Possible leakage of the gas system could affect the intensity of the peak m/z = 28 due to a possible contribution from

N_2^+. The absence of a peak intensity of m/z = 32 from the second air component (O_2) indicated that there was no leakage.

3. Theoretical methods

3.1. Molecular dynamics computations

The mass spectra of DHP at several different energies of the ionizing electron beam were simulated in the framework of the QCxMS method [59], [60]. The full technical details of QCxMS are given elsewhere [59], so here, we provide only a brief overview and relevant data for reproducing the present simulations. The basic principle of the method is the use of on-the-fly semi-classical molecular dynamics (MD) simulations with statistical initial conditions harsh enough to induce unimolecular fragmentation of the ionized molecule over several picoseconds MD duration time. The initial nuclear positions and velocities are sampled using random snapshots taken from a ground-state MD trajectory (the NVE ensemble). This preliminary MD run was propagated for 50 ps using the low-cost semiempirical tight-binding GFN-xTB method [61], [62]. To next simulate the process of the internal conversion from the initially highly excited state of the molecular ion to the ground state, the nuclear kinetic energies are scaled during the initial MD steps (the so-called heating phase) up to a preset value of the impact excess energy per atom (IEE). The heating time, here typically around 1.1 ps, depends explicitly on the ionized MO level and is an exponential function of the entire MO spectrum [59], here computed with GFN-xTB [61], [62]. Under these MD conditions, we propagated 1000 trajectories, each followed for up to 5 ps, using GFN-xTB for on-the-fly evaluation of energies and forces [61], [62]. This number of runs yielded sensibly converged mass spectra while still keeping the simulations feasible. For

the main MD runs, we additionally tested the ab initio PBE0/def2-SVP method [63], [64], although this was doable only with significantly fewer trajectories (250).

After the program detects that fragmentation has occurred along some MD trajectory, it assigns statistical charges to averaged structures of the fragments as a function of their ionization potential and internal temperature. The ionization potentials were computed at the spin-unrestricted ΔPBE0/def2-SVP [63], [64] level combined with the DFT-D4 scheme [65] for the dispersion correction. This procedure determines the probability of detecting a singly positively charged fragment in a given MD run in accordance with Stevenson's rule for competing fragmentations. The positions and intensities of the spectral lines are finally obtained by counting over all the detected fragments and taking into account the natural abundances of their isotopomers. The specific values of the adjustable parameters, viz., the impact energy of the electron beam (E_{imp}), the initial temperature of the vaporized DHP substrate (T_{init}), and the IEE used to simulate the mass spectra, are discussed in the Results section. The initial structure of the DHP molecule was obtained from the gas-phase MP2/cc-pVTZ optimization (the corresponding Cartesian coordinates and harmonic vibrational frequencies are given in the Supplementary Material). In all the simulations, the QCxMS program [59], version 5.2.1, was used and interfaced with the Orca 5.0.4 quantum chemistry suite [66], [67].

3.2. Machine learning simulations

The ionization cross section of DHP was estimated using a machine learning (ML) algorithm that was trained with measured ionization cross sections [68]. The full technical details of the ML algorithm are given elsewhere [68], and only a brief summary is provided here. A 3-layer, fully-connected, feed-forward network was trained using published experimental

datasets for 25 independent molecular targets. The network input was the target's chemical formula and the output was the total ionization cross-section as a function of projectile energy between 25 eV and 100 eV. The network was trained for 400,000 epochs, after which it was used to make a prediction of the total ionization cross-section for DHP. Extensive testing of the network and machine learning algorithm was previously performed, including the effects of different network structures, the number and identity of training molecules, and the number of epochs. This testing showed that the network's predictions for cross-sections of many different molecular targets were typically within 30% of the measured cross-section values and, in many cases, were within 10% of measured values. The chosen structure, number of training molecules, and number of epochs maximized the efficiency of the network while not sacrificing accuracy. The fully trained ML network of [68] was used to predict the DHP cross sections, and similar accuracy to that of [68] is observed here. Implementation of the network for prediction of the DHP cross-section took less than a second on a laptop computer, making the simulation highly efficient.

4. Results and discussion

4.1. Mass spectra of DHP

In order to identify the fragmentation processes and their products, the mass spectra of DHP were first measured with good statistics in the m/z = 10–90 mass range at the fixed electron energies of 12.5, 20, 25.5, 35, 70, and 100 eV. The original mass spectra are given in Figure S1 of the Supplementary Material. Here, the normalized mass spectra of DHP measured only at two electron energies of 12.5 and 100 eV are presented in Figures 2a and 2b, together with the assignments of the most intense mass peaks. These mass spectra were

corrected for the base background obtained by cutting off the DHP vapors (for background determinations, see supplementary material).

The present spectra can be compared with previous electron-impact study. Our mass spectra of DHP measured at 70 and 100 eV agree with the mass spectrum measured at 70 eV in the studies on low-temperature combustion performed by Koritzke et al. [52]. A low energy mass spectrum (shown in Figure S1 of the Supplementary Material) can also be compared with a preliminary study on the synchrotron radiation-induced DHP dissociation at 25.5 eV [69]. The photon-induced fragmentation spectrum shows a pattern similar to the mass spectrum obtained at the same electron energy. However, exposure to photons caused more severe fragmentation of the DHP parent cation than collisions with electrons, thus producing higher abundances of the low-mass fragments [69].

The theoretical mass spectra calculations were performed to interpret experimental spectral structures. Simulating and interpreting mass spectra through the QCxMS code has stirred significant interest due to its attractive combination of efficiency and accuracy [70], [71]. In the following, we discuss the performance of QCxMS in predicting the mass spectra of DHP at various energies of the electron beam. In particular, in-silico mass spectra after electron-impact ionization of DHP obtained from these MD simulations are shown in Figures S2-S4 of the Supplementary Material. Only the spectra directly corresponding to the measured spectra shown in Figures 2a and 2b are here shown in Figures 2c and 2d. The assignments of major cations and relative abundances of the mass peaks obtained from their intensities at 100 eV are listed in Table 1. Theoretically, dihydropyran can have several possible isobar cations at some observed masses. The assignments and percentages of all cations obtained from ab initio MD simulations (1000 runs) are listed in Table S1 in the Supplementary Material. The possible isobar cations can be formed in two ways. Firstly,

some isobars may come from different fragmentation pathways (e.g., $C_3H_6^+$ and $C_2H_2O^+$ at m/z = 42). Secondly, some isobar cations contain minor contributions from lower-mass ions because the natural composition of individual elements consists of small admixtures from the heavier isotopes (e.g., $C_3H_5O^+$ and $C_2H_4O^{13}C^+$ at m/z = 57). One can notice that both types of isobars often contribute to the intensity of a given mass peak, but at most masses, only one ion is dominant. Thus, the cations in Table 1 are chosen among the possible most intensive isobar cations. Moreover, only those fragmentation processes leading to the most abundant isobar are discussed in most cases.

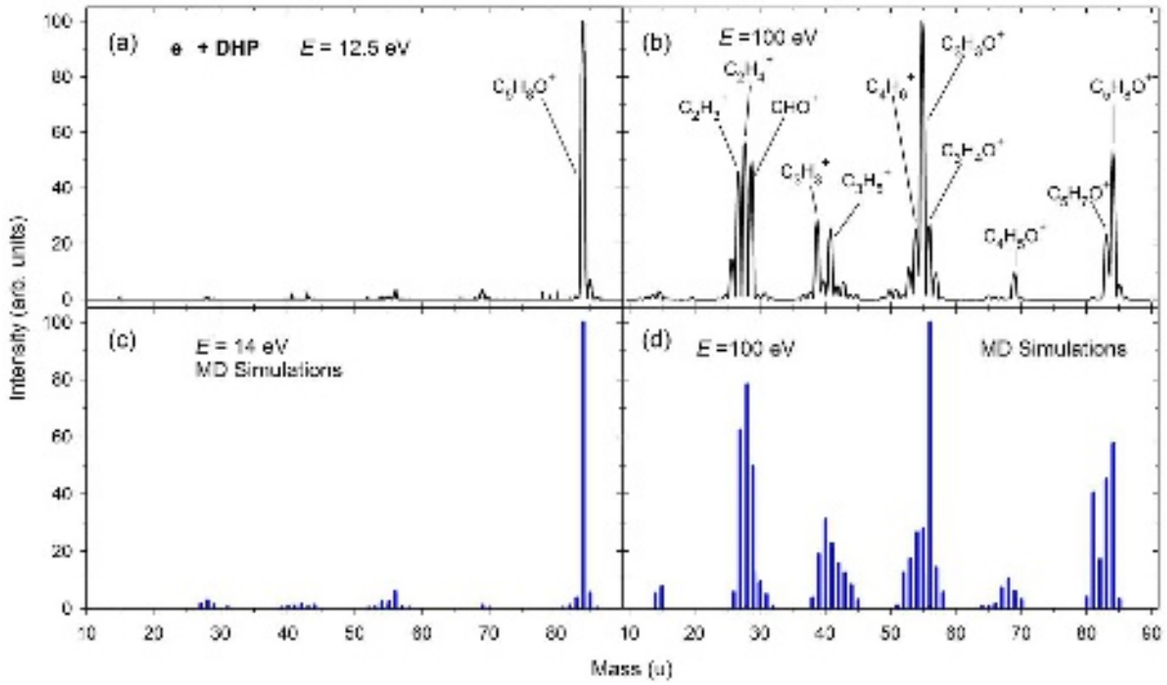

Figure 2. The normalized mass spectrum of the cations of DHP measured at the electron energy of a) 12.5 eV and b) 100 eV. The cation distribution obtained in the MD simulations for impact energy of c) 14 eV and d) 100 eV.

TABLE 1. The experimental (I_{Rel}) and theoretical (I_{Rel}^{Th}) relative intensities (in %) of cations obtained from DHP fragmentation at the electron energy of 100 eV. The most probable

assignments of significant cations and their percentages (in %) from MD simulations (1000 runs) are also given.

Mass (u)	I_{Rel} at E = 100 eV	I_{Rel}^{Th} at E = 100 eV	Cation assignment	Cation percentage
14	1.8	5.2	CH_2^+	100
15	2.8	7.5	CH_3^+	99.2
16	<1	-	O^+/CH_4^+	-
25	1.6	-	C_2H^+	-
26	14.7	5.6	$C_2H_2^+$	100
27	46.2	62.3	$C_2H_3^+$	99.8
28	56.3	78.2	$C_2H_4^+$	98.3
29	49.4	49.4	$C_2H_5^+$ / HCO^+	20.1 / 77.1
30	1.6	9.2	H_2CO^+	91.4
31	2.2	4.8	H_3CO^+	95.4
36	<1	-	C_3^+	-
37	1.6	-	C_3H^+	-
38	2.6	3.7	$C_3H_2^+$	100
39	28.4	18.8	$C_3H_3^+$	99.3
40	6.8	31.0	$C_3H_4^+$	98
41	25.5	22.7	$C_3H_5^+$	90.9
42	5.0	15.6	$C_3H_6^+$ / $C_2H_2O^+$	49.9 / 47.5
43	6.4	12.4	$C_3H_7^+$ / $C_2H_3O^+$	10.5 / 83.5
44	1.8	8.1	$C_2H_4O^+$	95.7
45	1.5	2.9	$C_2H_5O^+$	93.1
49	<1	-	C_4H^+	-
50	3.5	-	$C_4H_2^+$	-
51	3.5	1	$C_4H_3^+$	100
52	1.5	12.4	$C_4H_4^+$	99.6
53	11.4	17.4	$C_4H_5^+$	96.8
54	25.5	26.5	$C_4H_6^+$ / $C_3H_2O^+$	66.3 / 31.7
55	100.0	27.6	$C_4H_7^+$/ $C_3H_3O^+$	29.1 / 67
56	26.8	100.0	$C_3H_4O^+$	97.8
57	9.4	14.3	$C_3H_5O^+$ /$C_2H_4O^{13}C^+$	80.1 / 18.8
58	<1	5.5	$C_3H_6O^+$ /$C_2H_5O^{13}C^+$	88.1 / 7.7
65	1.3	<1	$C_5H_5^+$	94.6
66	1.1	1.6	$C_4H_2O^+$/ $C_5H_6^+$	32.9 / 65.3
67	<1	7.2	$C_4H_3O^+$	98.3
68	<1	10.0	$C_4H_4O^+$	96.9
69	9.6	6.1	$C_4H_5O^+$	92.7
70	<1	2.9	$C_4H_6O^+$/$C_3H_5O^{13}C^+$	90.5 /8.4
80	-	3.9	$C_5H_4O^+$	100
81	<1	40.4	$C_5H_5O^+$	99.5
82	<1	17.1	$C_5H_6O^+$/$C_4H_5O^{13}C^+$	88.3 / 11.5
83	23.3	45.1	$C_5H_7O^+$	97.7
84	52.9	57.5	$C_5H_8O^+$	95.8
85	5.3	3.1	$^{13}CC_4H_8O^+$	93.2

Firstly, we note that all the recorded signals appear in the simulated spectra (but the tables do not list the cations with too low intensities). However, there are notable discrepancies between the measured and predicted intensities that seemingly cannot be rectified in full within the QCxMS approach. We evaluate the performance based on a comparison of intensities between signals belonging to different groups of near-lying peaks ("inter-group") and the intensities within a given group ("intra-group").

Figure 2 shows that the inter-group intensities can be reproduced rather well upon choosing appropriate program settings. Thus, the simulation of the spectrum at the 100 eV beam energy correctly predicts the ordering of the six main groups of peaks by decreasing intensities: (1) m/z = 49-58; (2) m/z = 25-31; (3) m/z = 80-85 (containing the molecular ion at m/z = 84); (4) m/z = 36-45; (5) m/z = 65-70; and (6) m/z = 14-16.

For an optimal reproduction of the measured spectra, we found it beneficial to accompany the increasing E_{imp} energies with a suitable increase in the T_{init} and IEE parameters. For example, the values of T_{init} and IEE used to simulate the 100 eV spectrum (Figure 2d) were increased to 700 K and 1.0 eV/atom from the default values of 500 K and 0.6 eV/atom. Interestingly, the earlier GFN-xTB Hamiltonian used for the MD runs produced somewhat better spectra than the GFN2-xTB [72], although the differences between the two are not large.

However, such adjustments only bring about comparatively minor improvements. The most considerable improvement, contributing crucially to the well-predicted inter-group intensities, comes from completely suppressing the secondary fragmentation (i.e., setting the *maxsec* parameter to 0). In this way, possible further fragmentation of the primary fragments is not followed, and the distribution of the fragments appears to be statistical.

Neglecting the secondary fragmentation can finally render the correct ordering by the intensity of the m/z = 56, 28, and 84 signals, although precise reasons for this are not entirely clear. One hint is that the strongest signals at m/z = 55 and 56 are mostly due to the relatively fragile $C_3H_3O^+$ and $C_3H_4O^+$ fragments (compared, e.g., to the very robust $C_2H_4^+$ at m/z = 28), and so preventing the secondary fragmentation is beneficial for boosting their signals.

Note that Wang et al. [71] have recently shown that 37% of experimentally observed ions of several small molecules have no counterpart in the theoretical predictions because non-statistical rearrangement reactions leading to them were not recognized in the theory. In contrast, the interaction of DHP with electrons most likely leads to a non-statistical fragmentation of its ring, resulting in much more reactive fragments with a different intensity distribution than statistical fragmentation [73], [74]. This has been recently observed in the ionic impact with some simple hydrocarbons [75] and heterocyclic molecules [35], [37], [76], as well as collisions of heterocyclic molecules with VUV photons [26], [28].

The mass spectrum recorded in the vicinity of the ionization thresholds (at 12.5 eV) is also reproduced well (compare Figures 2a and 2c). The small value of E_{imp} (14 eV) was here accompanied by the suitably smaller IEE and T_{init} parameters of 0.15 eV and 200 K while again suppressing the secondary fragmentation.

On the other hand, much more significant discrepancies are seen with the intra-group intensities. These turned out to be persistent incorrigible errors, which make it meaningless to compare the predictions against the detailed intra-group ionization cross-sections (Figure S5). We still note that, upon passing the ionization threshold, the predicted spectra vary only little with the increase in the E_{imp} parameter, which is in line with the wide plateaus and mild changes seen in the partial cross-section plots.

The most important of the intra-group discrepancies is the assignment of the highest intensity signal to m/z = 56 instead of the observed m/z = 55. The corresponding dominating fragments differ by one H atom, which indicates that the incidence of the C–H bond scissions is significantly underestimated in the $C_3H_4O^+$ fragment. We note that this particular case of switched intensities cannot be rectified by allowing for secondary fragmentation. Moreover, despite the reduced number of the MD trajectories and consequently poorer statistics, we can also infer that the intra-group intensities cannot be improved by resorting to the ab initio (PBE0/def2-SVP) MD simulations. On the contrary, besides the still present m/z = 55/56 intensity switch, the molecular ion becomes erroneously attenuated (Figure S2). Thus, the huge computational cost of the KS-DFT MD, even for a comparatively small organic molecule such as DHP (10 days on 60 processors for the 250 runs), is not at all warranted.

Moreover, the m/z = 28 signal is regularly erroneously predicted as too intense compared to the m/z = 55/56 (Figure 2). Consequently, we wanted to test if such discrepancies could be caused by less reliable assignment of charges to this (and possibly other) co-fragment pairs. To this end, we tried other density functionals, viz. B3LYP [77], M06-2X [78], and CAM-B3LYP [79] in place of PBE0 [63] for obtaining the ionization potentials in the ΔDFT step. However, neither one of these functionals led to appreciable improvements for the inter-group intensities. Enlarging the basis set up to def2-TZVP was similarly found to be ineffective.

4.2. Absolute **total and partial ionization cross-sections**

In the second part of this work, the absolute total and partial electron ionization cross-sections of DHP were obtained. In these determinations, we used the mass spectra measured at 100 eV, the cation yield curves, and the relative flow technique [80] that

utilized the comparison of the intensity ratios of the ions from DHP to Ar^+ performed under identical experimental conditions of these products, thus giving the cross-sections relative to those for electron impact ionization of argon [81]. This method was previously successfully applied to determine absolute total and partial cross-sections for electron-impact ionization [80] and excitation [82] of the DNA bases.

In order to obtain the absolute total electron ionization cross-sections of DHP, the electron beam energy was kept constant at 100 eV. We maintained several pressures of the parent cation of DHP and Ar^+ in the range of $(0.6–4.2)\times10^{-6}$ mbar at this energy. The intensities of the m/z = 84 and m/z = 40 peaks of DHP and argon, respectively, were measured several times for different currents and recording times for each such pressure. In particular, argon measurements were performed immediately before and after each DHP run. Next, each intensity was normalized to electron beam current (in μA) and acquisition time (minute). The normalized intensities obtained for both targets were plotted as a function of pressure (see Figure 3). These dependencies are linear, thus indicating that molecular flow has been achieved over the pressure range studied. According to equation (2) in [80], a direct comparison of the slopes of the solid lines fitted to these experimental data points gives a relative level of the cross-sections. We obtained the $\sigma = (177\pm9)\times10^{-18}$ cm^2 cross-section for the production of the parent cation of DHP by using the standard cross-section of $(251\pm13)\times10^{-18}$ cm^2 [81] measured for Ar^+ at an incident electron energy of 100 eV. The error consists of the errors in the Ar^+ absolute cross-section determination [81], present experimental uncertainties, and the computed uncertainties involved in linear regression.

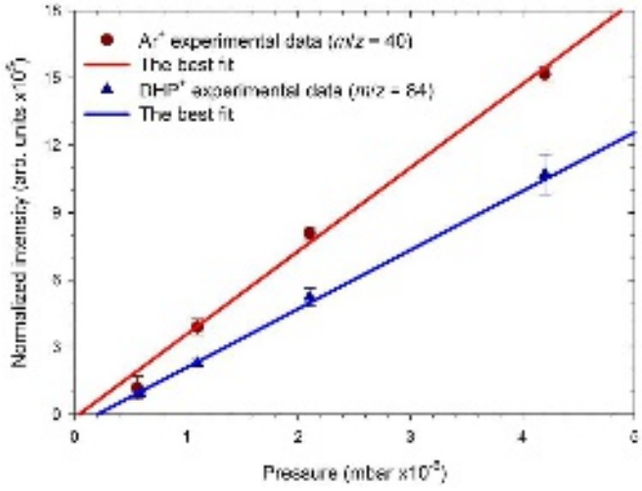

Figure 3. The normalized intensities of the m/z = 84 peak of DHP and m/z = 40 of argon versus pressures of these targets. The solid lines represent the best fittings.

The absolute total ionization cross-section at the 100 eV energy was found to be $(18.1\pm0.9)\times10^{-16}$ cm^2, and it was calculated from the ratio of the m/z = 84 peak intensity to the total intensity in the mass spectrum at an energy of 100 eV. This absolute total cross-section does not include contributions from H^+ and H_2^+ cations, which were omitted due to the difficulty of testing quadrupole transmission in this mass range. We have estimated that the contribution of both peaks to the absolute total cross-section is noticeable above an energy of 100 eV. Indeed, at an energy level of 70 eV, the contribution is 0.5 percent. The contribution is 2.1 and 2.6% at 100 eV and 140 eV, respectively. The effect of the underestimation of these peaks is, therefore, within the limits of the uncertainties.

Calculating the intensities of the other fragments (from the mass spectrum measured at 100 eV) relative to the total intensity allowed each cation to be placed on the absolute scale. All these ionization cross-sections obtained at the 100 eV energy are shown in Figure 4 and listed in Table 2.

TABLE 2. The obtained ionization cross-sections ($\sigma_{100\,eV}$) for producing the cations measured at 100 eV electron energy. The appearance energies E_{TH} (in eV) of the cations observed in the fragmentation of the DHP molecule after electron impact are also listed. The values in brackets represent the determined uncertainties.

Mass (u)	$\sigma_{100\,eV} \times 10^{-18}$ (cm^2)	E_{TH} (eV)
14	6.0 (0.3)	14.2 (0.6)
15	9.3 (0.5)	14.1 (0.1)
16	1.6 (0.1)	13.44 (0.05)
25	5.3 (0.3)	17.5 (0.1)
26	49 (2)	13.75 (0.03)
27	154 (8)	15.7 (0.1)
28	188 (9)	12.5 (0.3)
29	165 (8)	13.5 (0.2)
30	5.4 (0.3)	11.2 (0.9)
31	7.4 (0.4)	14.4 (0.3)
36	0.9 (0.1)	12.9 (0.9)
37	5.3 (0.3)	17.5 (0.5)
38	8.6 (0.4)	15.6 (0.1)
39	95 (5)	13.0 (0.2)
40	23 (1)	10.6 (0.3)
41	85 (4)	10.6 (0.2)
42	16.9 (0.8)	11.3 (0.5)
43	21 (1)	10.38 (0.04)
44	6.0 (0.3)	11.14 (0.07)
45	5.1 (0.3)	10.7 (0.3)
49	2.5 (0.1)	16.9 (0.1)
50	11.6 (0.6)	10.42 (0.08)
51	11.7 (0.6)	11.0 (0.2)
52	4.9 (0.3)	9.8 (0.1)
53	38 (2)	13.5 (0.1)
54	85 (4)	10.9 (0.3)
55	330 (20)	11.6 (0.1)
56	90 (4)	11.0 (0.2)
57	32 (2)	11.61 (0.06)
58	1.7 (0.1)	
65	4.3 (0.2)	12.66 (0.05)
66	3.7 (0.2)	11.3 (0.1)
67	2.0 (0.1)	
68	1.2 (0.1)	10.0 (0.8)
69	32 (2)	10.09 (0.03)
70	1.6 (0.1)	
81	2.5 (0.1)	10.6 (0.3)
82	0.8 (0.1)	
83	78 (4)	10.95 (0.05)

84	177 (9)	8.81 (0.03)
85	18 (1)	8.72 (0.03)
86	2.1 (0.1)	

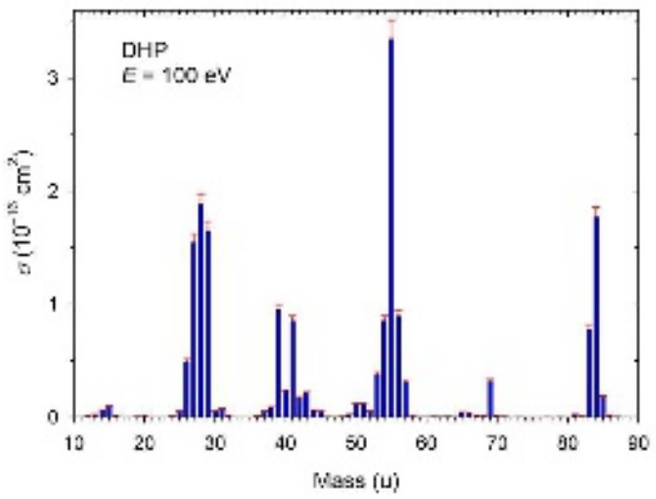

Figure 4. The ionization cross-sections (σ) at 100 eV as a function of cations' masses.

Electron impact ionization of DHP generates the parent ions and thirty-seven fragment cations with cross-sections larger than 10^{-18} cm^2 at 100 eV (see Table 2). For most of them, we could measure cation yield curves in the energy range from their respective thresholds to 140 eV. These yields were next put on the absolute cross-section scale using the ionization cross-section values at 100 eV ($\sigma_{100\ eV}$) presented in Table 2. The partial ionization cross-sections of some example cations, namely $C_5H_8O^+$ (84 u), $C_5H_7O^+$ (83 u), $C_4H_5O^+$ (69 u), $C_4H_7^+/C_3H_3O^+$ (55 u), and $C_2H_4^+$ (28 u) measured in the 5-140 eV energy range are displayed in Figure 5. The partial ionization cross-sections of all cations are shown in Figure S5 of the Supplemental Material. Generally, the cross-section curves rise quickly above the thresholds up to maximal values, and then, depending on the cation, they reach the plateau or decrease slightly. As seen from these figures, the production of parent cation $C_5H_8O^+$ governs the dissociative ionization of DHP in the energy range of 9.8-18 eV. Above 18 eV, m/z = 55 cation generation becomes the major fragmentation channel.

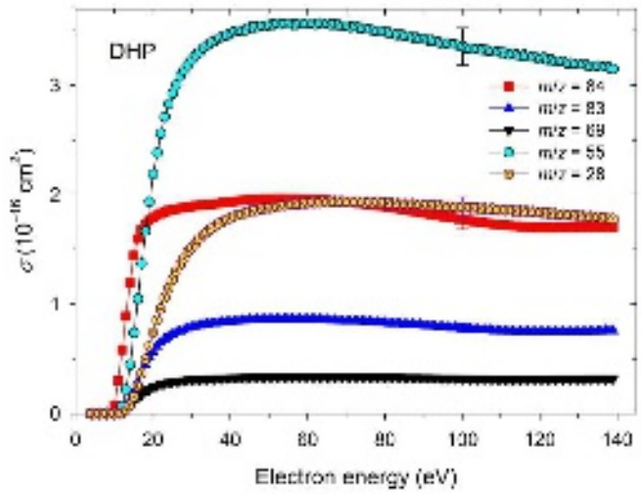

Figure 5. The partial ionization cross sections for some characteristic cations of DHP measured in the electron energy range of 5–140 eV.

The sum of all partial cross-section curves gave the energy dependence of the total ionization cross-sections displayed in Figure 6 and listed in Table 3. The cross-section at 100 eV is one percent lower than $(18.1\pm0.9)\times10^{-16}$ cm^{2,} most likely due to the absence of partial cross-section curves for fragments of negligible intensity in this summation.

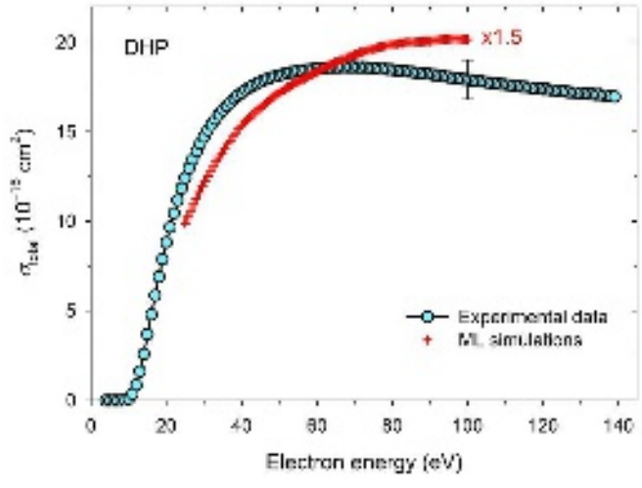

Figure 6. Total ionization cross-sections of DHP measured in the electron energy range 5–140 eV in the present measurements (circles) and calculated using machine learning simulations (crosshairs).

Because of the lack of cross-section determinations involving DHP molecules that have been studied, no direct comparison could be made to literature data. Present experimental total ionization cross-sections may be, however, compared with electron-induced total ionization cross-sections for similar six-membered rings of pyridine [83], pyridazine [55], and pyrimidine [84]. The comparison is somewhat rough because these molecules contain nitrogen heteroatoms in their structures instead of oxygen and thus are characterized by different nuclear and electronic complexity. Nevertheless, these results may shed light on the general trends in the current curve and the order of magnitude of present cross-sections. Particularly, the cross-section curves obtained for all these molecules do not rise as rapidly as the total cross-section curve of DHP. They have lower values than the present ones, but the order of magnitude of these cross-sections is the same as our results. Indeed, the total cross-section curve shown in Figure 6 reaches a maximum of 18.6×10^{-16} cm^2 at 67 eV. In contrast, the highest ionization cross-sections of pyridine and pyridazine appear at about 90 eV and are equal to 15×10^{-16} cm^2 [83] and 12.7×10^{-16} cm^2 [55], respectively. The maximum value of the pyrimidine ionization cross-section appears at 85 eV but is twice as low as a result obtained for DHP [84].

In the next step of our studies, we performed machine learning calculations to check the present observations. The results of these simulations performed in the 25-100 eV energy range are presented in Figure 6 and provided in Table 3. In Table 3, we only listed the cross-sections calculated for measured energies and omitted the results simulated for any others. The agreement between prediction and experiment is satisfactory. The ML simulations underestimate the experimental cross-sections at lower electron energies by about 46%. This underevaluation decreases gradually, and it reaches 25% at 100 eV. The machine-learning model recently predicted ionization cross-sections for various molecular

targets, including ring structure heterocycles, such as pyridine, pyrimidine, and nucleotide bases (see Ref. [68]). ML simulations underestimated the experiment by about 29% for pyridine, but for pyrimidine, they, in contrast, overestimated the experiment by 13% at 100 eV [68].

The shape and magnitude of the predicted ML cross-sections are dependent on the cross-sections used to train the network. Because the network was trained to associate the cross section (network output) with the chemical formula of the molecular target (network input), its predictions for unseen molecules will resemble those of molecules with similar chemical formulas. Here, the ML-predicted DHP cross-section does not show a maximum as is observed in the measured cross-section. This is likely due to the fact that only one of the network training datasets (ethanol) exhibited a maximum in the cross-section at less than 100 eV. Because the other training datasets, including those for molecules with chemical formulas similar to DHP, did not have a maximum at less than 100 eV, the algorithm was unable to predict the maximum in the DHP cross-section.

Similarly, the cross sections for molecules with similar chemical formulas to DHP (e.g., butanone, C_4H_8O or pentan-2-one, $C_5H_{10}O$) have smaller magnitudes than that measured for DHP. This causes the algorithm to underestimate the DHP magnitude. We note that no cross-sections for ring molecules (such as pyridine or pyrimidine) were included in the training data for the network. However, including these molecules in the algorithm's training is unlikely to have significantly improved the prediction of the location of the DHP cross-section maximum since these molecules exhibit maxima near 90 eV, unlike at 67 eV for DHP. The inclusion of ring molecules in the training datasets is also unlikely to have improved the prediction of the magnitude of the DHP cross-sections since the algorithm's prediction for DHP already falls between the maximum cross-section for pyridine and pyrimidine.

As noted above, pyridine, pyrimidine, and DHP have similar structures but different nuclear constituents. Yet, their cross-sections exhibit different magnitudes and maxima locations, indicating that the nuclear composition of the molecule influences the ionization cross-section. In contrast, the ML algorithm includes the nuclear composition of the molecule but not its molecular structure and likewise predicts ionization cross-sections with different magnitudes and maxima locations. Combined, this underscores the need to account for both the nuclear composition and the structure of the molecule in theoretical simulations.

TABLE 3. Experimental (σ) and simulated (σ_{ML}) total ionization cross-sections of DHP obtained in the electron energy range of 8–140 eV.

E (eV)	$\sigma\times10^{-16}$ (cm^2)	$\sigma_{ML}\times10^{-16}$ (cm^2)	E (eV)	$\sigma\times10^{-16}$ (cm^2)	$\sigma_{ML}\times10^{-16}$ (cm^2)	E (eV)	$\sigma\times10^{-16}$ (cm^2)	$\sigma_{ML}\times10^{-16}$ (cm^2)
8	0.0		53	18.3		98	18.0	
9	0.001		54	18.3		99	17.9	
10	0.08		55	18.4	11.9	100	17.9	13.4
11	0.36		56	18.4		101	17.9	
12	0.9		57	18.4		102	17.8	
13	1.6		58	18.5	12.1	103	17.8	
14	2.6		59	18.5		104	17.8	
15	3.7		60	18.5		105	17.8	
16	4.8		61	18.5	12.3	106	17.7	
17	5.9		62	18.5		107	17.7	
18	6.9		63	18.6		108	17.7	
19	7.9		64	18.6	12.5	109	17.6	
20	8.8		65	18.6		110	17.6	
21	9.7		66	18.6		111	17.6	
22	10.5		67	18.6	12.7	112	17.6	
23	11.2		68	18.6		113	17.6	
24	11.8		69	18.6		114	17.5	
25	12.4	6.6	70	18.6	12.9	115	17.5	
26	13.0		71	18.6		116	17.5	
27	13.5		72	18.6		117	17.5	
28	13.9	7.5	73	18.6	13.0	118	17.4	

29	14.3		74	18.6		119	17.4	
30	14.7		75	18.5		120	17.4	
31	15.1	8.3	76	18.5	13.1	121	17.4	
32	15.4		77	18.5		122	17.3	
33	15.7		78	18.5		123	17.3	
34	16.0	9.0	79	18.5	13.2	124	17.3	
35	16.2		80	18.5		125	17.3	
36	16.4		81	18.4		126	17.2	
37	16.6	9.8	82	18.4	13.3	127	17.2	
38	16.8		83	18.4		128	17.2	
39	17.0		84	18.4		129	17.2	
40	17.2	10.3	85	18.3	13.3	130	17.2	
41	17.3		86	18.3		131	17.1	
42	17.5		87	18.3		132	17.1	
43	17.6	10.6	88	18.3	13.4	133	17.1	
44	17.7		89	18.2		134	17.1	
45	17.8		90	18.2		135	17.1	
46	17.9	11.0	91	18.2	13.4	136	17.0	
47	18.0		92	18.2		137	17.0	
48	18.0		93	18.1		138	17.0	
49	18.1	11.4	94	18.1	13.4	139	17.0	
50	18.2		95	18.0		140	17.0	
51	18.2		96	18.0				
52	18.3	11.6	97	18.0	13.5			

4.3. Appearance energies

During determinations of the cross-section curves, we performed more detailed measurements close to the expected thresholds of identified cations to obtain their appearance energies (E_{TH}). Specifically, each threshold energy was obtained by fitting a modified Wannier function [85] to experimental points employing the "ThreSpect" code [86], which is available in the Most Wiedzy Open Research Data Catalog (i.e., the Gdansk University of Technology Bridge of Knowledge repository) [87]. This procedure has recently been successfully applied to get the appearance energies of cations produced in electron-induced single ionization and fragmentation of pyridine [54] as well as two-body dissociation channels detected in the photo-double-ionization of the isoxazole molecules [23].

All the fittings to the near-threshold cross-sections of identified cations are tabularized in Table S2 of the Supplemental Material. Here, only some example patterns of such experimental and fitted curves are shown in Figure 7. The obtained E_{TH} of DHP cations and their uncertainties are given in Table 2. Although our MD calculations suggest the possibility of producing several isobar cations at some observed masses (see Table S1 of the Supplemental Material), our cross-section curves do not show additional thresholds at higher electron energies.

Because works concerning electron-induced ionization studies of DHP are scarce, no direct comparison can be made to the literature data. Our results can only be compared with ionization energy referenced by NIST [56]. Because our ionization energy was derived from the fittings to the cross-section curves of the m/z = 84 and 85 cations, we calculated a weighted mean value of these results equal to 8.76 (0.02) eV. This value is 0.41 eV higher than the recommended value of 8.35 (0.01) eV, which was evaluated by NIST [56] from four literature results [88]-[91] determined by photoelectron and photoionization techniques.

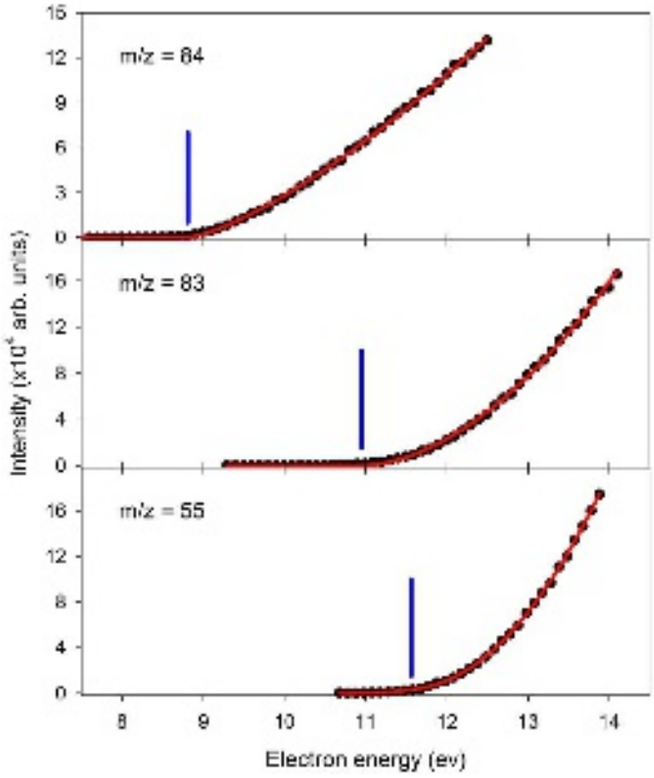

Figure 7. The cross-sections measured near the expected threshold regions (black points). The solid red lines display the best fittings to the experimental data. The vertical blue bars represent the positions of the E_{TH} energies.

4.4. Fragmentation channels

The observed fragmentation mechanisms may be complex, considering the high amount of energy deposited into a molecule during energetic collisions. It is well-known that molecules may distribute the absorbed energy into several degrees of freedom and thus may not decay by simple bond rupture but may be subjected to substantial rearrangement deformation of the bond structure via isomerization. Subsequently, isomerization may lead to the opening of new reaction channels, which frequently include dissociation. Such processes have been demonstrated for several five- and six-membered heterocyclic molecules (for example, isoxazole [28], furan [76], tetrahydrofuran [92], or pyridine [26],[37]) and, as the calculations

show, may also appear in the DHP dissociation. The possible fragmentation pathways leading to fragments within each group of peaks are discussed below.

4.4.1. Fragments with m/z = 80-85

The heaviest group is formed by the parent cations m/z = 84 and 85, and one ionic fragment m/z = 83, generated by a single dehydrogenation of the DHP parent cation. As seen in Table 2, the $C_5H_7O^+$ is not the first cationic fragment to arise. Thus, the hydrogen elimination, which preferentially produces the α-radical with the radical site on the C(6) carbon atom, is not such a simple rupture, but it likely involves a DHP ring opening and the migration of the hydrogen atoms before H abstraction. The studies on tetrahydropyran fragmentation suggest that such an α-radical is also prone to ring-opening due to low C-O bond energy (3.7 kcal/mol) [51].

The MD simulations show that m/z = 84 and 83 are indeed the strongest, but contrary to the experiment, calculations additionally predicted intensive cations with masses m/z = 82, 81, and 80 corresponding to $C_5H_6O^+$, $C_5H_5O^+$, and $C_5H_4O^+$, respectively. This result may suggest the possibility of DHP fragmentation via the shake-off dehydrogenation mechanism. Very recently, such a reaction has been observed experimentally in the electron-induced dissociative ionization of pyridine, the six-membered heterocyclic molecule containing nitrogen instead of the oxygen atom [54]. This mechanism occurs via the sequential abstraction of hydrogen atoms from the parent cation or its fragmentation products as far as they can form cyclic stable structures [54]. The minor intensities of m/z = 80-82 peaks in experimental mass spectra (see Table 1) may suggest that the DHP parent ion cannot form such resonance structures and undergoes rapid decomposition immediately after sequential dehydrogenation. Pyridine could form such structures because three C=C

bonds stabilize its ring. DHP has only one C=C bond in its cyclic structure (Figure 1), and its five single bonds are vulnerable to ruptures.

4.4.2. Fragments with m/z = 65-70

The differences in the two spectra shown in Figure 2 for the second heaviest group are slightly different than for the m/z = 80-85 cation group. Apart from the m/z = 69 peak, all other cations of this group have negligibly low intensities on the measured mass spectrum (see Table 1 and Figure 2). On the contrary, theoretical intensities vary from 1.6 to 10%, with the maximum at m/z = 68.

The fragments with m/z = 68 and 69 masses appear at the lowest energies among those with m/z = 65-70. The appearance energies of these cations lie around 10 eV (Table 2). The cross-section for the formation of the most intense fragment, m/z = 69, is an order of magnitude higher than that of the other fragments in this group. The formation of the m/z = 69 cation requires the opening of the DHP ring by cleavage of the O(1)-C(6) single bond, hydrogen migration to C(6), and rupture of the C(5)-C(6) bond, leading to the final reaction products:

$$e^- + C_5H_8O^+ \rightarrow C_4H_5O^+ + CH_3 + 2e^-. \quad (1)$$

The fragment with m/z = 68 mass is likely produced in a similar reaction, but it further requires hydrogen removal from $C_4H_5O^+$, leading to the formation of the $C_4H_4O^+$. An additional hydrogen abstraction from $C_4H_4O^+$ may produce $C_4H_3O^+$ (m/z = 67). MD calculations suggest that cations with m/z = 65 and 66 masses may be produced in alternative reactions occurring via the detachment of $(H_2O+H)/(OH+2H)/(O+3H)$ or $H_2O/(OH+H)/(O+2H)$, respectively, giving:

$$e^- + C_5H_8O^+ \rightarrow C_5H_5^+ + (H_2O+H)/(OH+2H)/(O+3H) + 2e^-, \quad (2)$$

$e^- + C_5H_8O^+ \rightarrow C_5H_6^+ + H_2O/(OH+H)/(O+2H) + 2e^-$. (3)

However, these reactions are more complex than those arising according to the scheme (1) and are, therefore, less likely to occur.

4.4.3. Fragments with m/z = 49-58

Ten peaks can be detected in the m/z = 49-58 mass region. The MD calculations suggest two different decomposition channels leading to the formation of these fragments. Both processes may start with opening the parent cation ring structure by O(1)-C(6) bond cleavage, followed by bond rearrangements and the intramolecular migration of hydrogen atoms from one molecular site to another. Then, the production of the three heaviest fragments in this group occurs via C(4)-C(5) single bond rupture, leading to the reactions:

$e^- + C_5H_8O^+ \rightarrow C_3H_4O^+ + C_2H_4 + 2e^-$, (4)

$e^- + C_5H_8O^+ \rightarrow C_3H_5O^+ + C_2H_3 + 2e^-$, (5)

$e^- + C_5H_8O^+ \rightarrow C_3H_6O^+ + C_2H_2 + 2e^-$. (6)

The most straightforward process is the one leading to the formation of a m/z = 56 cation, i.e. (4). It requires only the opening of the DHP ring and the rearrangement of the bonds in the resulting open-structure cation, followed by C(4)-C(5) cleavage. This mechanism is in agreement with low-temperature thermal decomposition investigations of neutral DHP, which identified acrolein (O=CH-CH=CH_2) and ethylene (CH_2=CH_2) as the main pyrolytic products [93], [94]. Pyrolysis leads to the primary fragmentation products without secondary fragmentation. These primary products most likely correspond to the skeletal fragments resulting from the statistical disintegration of the ring. Interestingly, using acrolein as the primary substrate in the catalytic asymmetric inverse-electron-demand oxa-Diels–Alder

reaction leads to the formation of 3,4-dihydropyran having an unoccupied C(6) position in its ring structure [95] thus suggesting the importance of the (4) pathway.

Reactions (5) and (6) require additional migration of one or two hydrogens, respectively, and are thus less probable, which is in agreement with observed partial cross-sections for the production of these cations (see Table 2). It remains an open question whether DHP can decompose by breaking two single bonds, O(1)-C(2) and C(3)-C(4), leading directly to the formation of the products shown in reaction (6). This pathway would start by breaking a bond stronger than the very weak O(1)-C(6), which is probably connected with a higher activation barrier. Indeed, Koritzke et al. [52] suggested that oxygen O(1) and possibly carbon C(3) are putative ionization sites. In the first situation, this weakens the O(1)-C(6) bond, and in the second, the C(2)=C(3) bond. Therefore, the channel through O(1)-C(2) and C(3)-C(4) scission is less probable than decomposition via the reaction (6).

Transannular cleavage is the second mechanism that starts from the O(1)-C(6) bond rupture. This process leads to the formation of the five lightest cations in the m/z = 49-58 mass group via C(2)=C(3) double-bond cleavage accompanied by hydrogen transfers. The course of this reaction can be facilitated because the ionization site can be the C(3) carbon, causing the initial cleavage of one of the two bonds between C(2) and C(3) [52]. The appearance energy of the m/z = 52 cation is the lowest of all the fragments. This may indicate a favorable decay of DHP through this mechanism. Abundances of the m/z = 51-53 cations obtained in MD calculations also suggest the reliability of this picture. Our experiment detected further cations with masses m/z = 49 and 50 absent in the theoretical mass spectrum. We assign these fragments to the production of the C_4H^+ and $C_4H_2^+$, respectively.

The peaks at m/z = 55 and 54 most likely consist of isobaric cations generated competitively by both fragmentation processes, as shown in Table 1. In particular, Koritzke et al. [52] suggested that a m/z = 55 fragment may be created as a hydrocarbon cyclobutyl cation ($C_4H_7^+$). Conversely, the $C_4H_7^+$ fragment contributing 29.1% to the m/z = 55signal (Table 1) is not as frequent because its direct formation involves the scission of the double C2=C3 bond, which is less probable. According to the MD simulations, the first pathway, namely:

$$e^- + C_5H_8O^+ \rightarrow C_3H_3O^+ + (C_2H_5)/(H+C_2H_4) + 2e^- \quad (7)$$

is more probable in producing the m/z = 55 ion. Indeed, the theoretical abundance of the $C_3H_3O^+$ ion equals 67% (see Table 1). For the production of the m/z = 54 cation, the transannular cleavage mechanism begins to predominate, resulting in a reversed situation: the $C_4H_6^+$ hydrocarbon fragment is produced with a probability of 66.3% and the $C_3H_2O^+$ cation with a probability of 31.7%.

Reaching the fragments in the m/z = 49-58 mass group by ring opening through the O(1)-C(2) bond break may require more complicated ring rearrangements and the collective movements of several hydrogen atoms. However, Koritzke et al. [52] suggested that this site may be exposed to inductive cleavage, initiating fragmentation of DHP into lower mass fragments rather than heavier species. Nevertheless, the fragmentation channels starting from the O(1)-C(2) bond rupture and giving the peaks with the m/z = 49-58 masses cannot be excluded.

4.4.4. Fragments with m/z = 36-45

In this mass region, we detected ten peaks. Cations with m/z = 39 and 41 masses are the strongest and have relative intensities equal to 28 and 25.5%, respectively. Other

fragments in this mass region have relative intensities lower than 7%. In contrast, calculations show that the peak corresponding to a mass of m/z = 40 is the most intense (I_{Rel}^{Th} at E = 100 eV equals 31%), while the other peaks form steadily decreasing "wings" on both sides of this cation.

According to MD predictions, the lower mass fragments in this mass group consist of a sequence of hydrocarbon cations having three carbon atoms, while higher mass fragments contain the carbonyl group. As in the case of decomposition leading to fragments with masses of m/z = 49-58, there may also be two dominant decay processes generating these cations. Again, both processes would depend on the ionization site. If it is oxygen, the decomposition most likely occurs via breaking the O(1)-C(6) and C(3)-C(4) bonds, yielding a sequence of cations having oxygen. If it is the carbon C(3) site, the inductive effect may prevail, leading to a hydrocarbon series by breaking the O(1)-C(2) and C(4)-C(5) bonds. Naturally, both processes should occur with simultaneous hydrogen migrations.

For example, inductive cleavage of the O(1)-C(2) single bond, accompanied by the open ring structure rearrangement followed by α-cleavage has been proposed [52] to yield the allene cation ($C_3H_3^+$) corresponding to the most intense peak (39 u) in this mass range at the experimental spectrum (Figure 2b). The appearance energy of this fragment is 13 eV, corroborating the complexity of the underlying reaction. From a theoretical point of view, it would be much simpler to have an inductive mechanism of scission across the ring starting from O(1)-C(2) followed by C(4)-C(5) bond cleavage. Such a process will likely yield the $C_3H_4^+$ cation, which is calculated to be the most abundant in this mass range. In addition, the appearance energy of this fragment is relatively low (10.6 eV), which makes the above considerations plausible. The hydrogen transfers from one side to the other prior to inductive scission across the ring can alter the course of this reaction, thus making this

process increasingly complicated. Therefore, lower- and higher-mass hydrocarbon fragments have diminishing abundances in the theoretical mass spectrum (Figure 2d) and, experimentally, have increasing appearance energies (see Table 2). Our calculations imply that this mechanism is probably responsible for the efficient production of cations with masses as high as m/z = 43. Moreover, our experiment detected very low-intensity cations with m/z = 36 and 37 masses, missing in the theoretical mass spectrum. We assign these peaks to the production of the C_3^+ and C_3H^+, respectively.

The formation mechanism of oxygen-containing cations complements the DHP decay scenario via the inductive effect presented above. Such fragments can be produced by a straightforward decomposition process that covers the m/z = 42-45 mass region. In particular, a cation with m/z = 42 mass is likely formed by transannular cleavage across the DHP ring, which would involve O(1)-C(6) rupture followed by C(3)-C(4) bond scission. This mechanism splits the DHP ring into precisely two m/z = 42 moieties, C_3H_6 and C_2H_2O. With respect to the ionization site, this process leaves the C_2H_2O in a charged state. Transannular cleavage across the DHP ring seems to be a simple decomposition mechanism, but the appearance threshold of the m/z = 42 cation is surprisingly high, and the cross-section is low (see Table 2).

Similarly to the production of cations m/z = 54 and 55, fragments m/z = 42 and 43 formation is also affected by an interchange of fragmentation processes. Our calculations suggest that a second isobar with the mass m/z = 42, namely $C_3H_6^+$, also contributes to the abundance of the m/z = 42 peak. Actually, both isobars contribute almost equally to this peak (see Table 1). Here, the inductive effect occurring via O(1)-C(2) and C(4)-C(5) bond breakage accompanied by extensive rearrangement of the DHP skeleton may produce $C_3H_6^+$ cation. On the other hand, the transannular cleavage mechanism dominates the formation

of the m/z = 43 cation, leading to an 83.5% probability of forming the $C_2H_3O^+$ fragment. The MD calculations suggest that the probability of forming the $C_3H_7^+$ hydrocarbon isobar is only 10.5%.

4.4.5. Fragments with m/z = 25-31

This mass region consists of intensive m/z = 27-29 peaks (Table 1). The m/z = 28 is well reproduced as the strongest in MD simulations (Table 1). Theoretical intensities of m/z = 27 and 29 cations are also satisfactorily predicted.

Our MD predictions again show that the lower mass fragments in this mass group consist of a sequence of hydrocarbon cations (but having two carbon atoms), while higher mass fragments contain the CO moiety. Hydrocarbons likely correspond to ethynyl (25 u), acetylene (26 u), vinyl radical (27 u), and ethylene (28 u) cations, respectively. Oxygen-containing fragments are possibly the formyl cation (HCO^+), formaldehyde cation (H_2CO^+), and methoxy cation (CH_3O^+).

These cations may be formed in reactions similar to those producing fragments with masses of m/z = 49-58. However, the appearance energies are here considerably higher (see Table 2), implying the existence of some factors that complicate the processes leading to the formation of the m/z = 25-31 fragments as charged counterparts of the m/z = 49-58 fragments. The first factor may be the ionization site. It may differ from the ones previously proposed, thus increasing or decreasing the energies of the individual bonds. Secondly, the ionization site may be the same, but forming low-mass cations requires intramolecular charge transfer from one molecular site to another before the bonds are ruptured. The second factor seems more probable. This may be indicated by the calculated percentage of individual cations (see Table 1), which corresponds to the percentage of heavy mass

partners. In addition, the peak corresponding to the m/z = 29 fragment is expected to be a combination of signals from two cations, i.e., $C_2H_5^+$ and HCO^+. Similarly, its heavier partner (m/z = 55) likely comprises two remaining moieties of the DHP ring ($C_3H_3O^+$ and $C_4H_7^+$, as seen in Table 1). Furthermore, a change in the fragmentation mechanism is evident in the production of both fragments.

We can, therefore, conclude that the transannular cleavage mechanism starting from the O(1)-C(6) bond rupture followed by C(2)=C(3) double-bond cleavage accompanied by charge and hydrogen transfers may lead to the formation of the three heaviest cations in the m/z = 25-31 mass group. The lighter cations may be generated in processes starting again with opening the parent cation ring structure by O(1)-C(6) bond cleavage, but followed by the intramolecular charge and hydrogens migration and scission of the C(4)-C(5) bond similarly to reactions (4)-(6). Both fragmentation pathways may participate in creating the formyl cation (29 u).

4.4.6. Fragments with m/z = 14-16

This mass region consists of the lightest cations. The peak with the mass of m/z = 16 is the fragment that originates at the lowest energy in the m/z = 14-16 region. The E_{th} of this cation was found to be 13.44 (0.05) eV. This peak is visible in the MD simulations. However, it is very weak, and we have not included it in the present tables. It is predicted to be primarily due to CH_4 (43%) and $^{13}CH_3$ (55%), so oxygen production can be excluded.

The cations with masses m/z = 14 and 15 arise at the energy of 14.1-14.2 eV and are almost four and six times more intensive than the m/z = 16 peak. According to the MD predictions, the most intense peak belongs to the CH_3^+ cation produced in the reaction:

$$e^- + C_5H_8O^+ \rightarrow CH_3^+ + C_4H_5O + 2e^-. \quad (8)$$

The CH_3^+ cation may be formed by an alternative mechanism to the (1) reaction, suggesting the same intermediate state for processes (1) and (8). However, the difference in the cross-sections and appearance energies may imply that ring rearrangement leading to CH_3^+ is more complex than the $C_4H_5O^+$ cation. Indeed, the observation of the CH_3^+ cation, which is not a structural component of the DHP molecule, is direct experimental proof for the migration of hydrogen atoms along the ring prior to fragmentation.

The lightest fragment (i.e., m/z = 14) in this mass range is assigned to the CH_2^+ formation (see Table 1). The fragmentation mechanism leading to the CH_2^+ formation seems to be quite simple, consisting of a rupture of two O(1)-C(6) and C(6)-C(5) single bonds. The same reaction may produce the m/z = 70 cation. However, the cross-sections for the production of both these cations are very low, and the E_{TH} of CH_2^+ is relatively high, thus suggesting a rather high energy barrier for this process.

It is noteworthy that the MD calculations did not predict the generation of the atomic fragments. Even if such cations were generated, they would have a minor contribution to the production of the m/z = 12 and 16 fragments due to complex, energy-consuming fragmentation channels, which lead to the complete disintegration of the DHP ring structure. This is perhaps why we did not detect the peak corresponding to the mass of m/z = 12. If such atomic fragments were formed in excited states, their fluorescence could be directly detected and identified in the emission fragmentation spectra. However, the emission fragmentation spectra of similar five-membered heterocyclic molecules (e.g., pyrrole [15], tetrahydrofuran [21], and pyridine [28]) obtained using electron- or photon-induced fluorescence spectroscopies showed no emission from atomic fragments, corroborating our supposition.

5. Conclusions

The dissociative ionization of 3,4-dihydro-2H-pyran was studied using electron-induced mass spectrometry combined with molecular dynamics and machine learning simulations. Using a quadrupole mass spectrometer, we recorded the mass spectra in the m/z = 10–90 mass range for 8-140 eV electron energies. These spectra revealed 41 mass peaks that could be assigned to particular cations using theoretical molecular dynamics calculations.

Guided by these calculations and in conjunction with other dissociation measurements, the fragmentation mechanisms were suggested. Generally, the fragmentation pathways of DHP observed along the MD trajectories are rather complex and do not seem to exhibit readily recognizable or systematic patterns. The mechanisms typically involve recurrent bond breakings and formations and a sequence of rearrangements before the fragments definitively split. In particular, the electron-induced fragmentation mechanisms of DHP depend on the site at which the molecule is ionized. Two sites are mainly prone to electron attack: oxygen O(1) and carbon C(3). When DHP is ionized at the O(1) site, the O(1)-C(6) bond breaks as the first one, followed by the C(5)-C(6), C(4)-C(5), and C(3)-C(4) bonds break depending on how massive the fragment is formed, and accompanied by charge and/or hydrogen migrations. This process may compete with the transannular cleavage mechanism, which starts from ionization at the C(3) site followed by the initial cleavage of the O(1)-C(6) bond and one of the two bonds between C(2) and C(3). There is an inversion between these processes for most mass groups. This inversion of the fragmentation mechanisms remains somewhat puzzling at the moment, but our results clearly show that it happens.

We have also determined the total and partial ionization cross-sections of 37 cations in the energy range from their respective appearance energies (E_{TH}) to 140 eV. To complete the above results, we have performed machine learning simulations predicting total ionization cross-sections. Comparing the simulation data with the experimental values showed a satisfactory agreement, similar to previous predictions made using the ML algorithm.

The measured cross-sections show that the production of parent cation $C_5H_8O^+$ starts at 8.76 (0.02) eV, and it governs the dissociative ionization of DHP at lower energies. However, above 18 eV, m/z = 55 cation becomes the primary fragmentation product.

The present results can shed light on the fragmentation of cyclic ether intermediates involved in degenerate chain branching in low-temperature hydrocarbon oxidation and biofuel combustion. Moreover, these results may be used as the input data in radiation-induced damage models to improve radiation treatment protocols. Indeed, the electron-induced ionization cross-sections of DHP are higher than those measured for similar six-membered heterocyclic molecules containing nitrogen atoms. MD calculations suggest that DHP decomposes into many reactive oxygen-containing fragments with high cross-sections. This could pave the way for producing efficient oxygen-rich radiosensitizers containing DHP rings. The reactive oxygen species formed after irradiation of such drugs may alter cancer cells more severely, thereby increasing their therapeutic potential.

Supplementary Material

The supplementary material includes detailed description of experimental procedures and conditions; Cartesian coordinates (Å) and harmonic vibrational wavenumbers (cm^{-1}) of the DHP minimum optimized at the MP2/cc-pVTZ level; the original mass spectra of DHP

measured after electron collisions (Fig. S1); the ab-initio MD (PBE0/SVP) simulated mass spectra of DHP at the different impact energies (Figs. S2-S4); the assignments of all cations and their percentages (in %) from MD simulations (Table S1); the ionization cross sections for the specified cations of DHP measured in the electron energy range of 5–140 eV (Fig. S5); experimental cross-sections and simulations near thresholds (Table S2).

Acknowledgments

This article is based upon work from COST Action CA20129 − Multiscale Irradiation and Chemistry Driven Processes and Related Technologies, supported by COST (European Cooperation in Science and Technology). The work of I. Lj. was supported in full by the Croatian Science Foundation under the project numbers IP-2020-02-9932 and IP-2022-10-4658.

References

[1] G. Danaei, S. V. Hoorn, A. D. Lopez, C. J. L. Murray, M. Ezzati, Causes of cancer in the world: comparative risk assessment of nine behavioural and environmental risk factors, Lancet **366**, 1784–1793 (2005). https://doi.org/10.1016/S0140-6736(05)67725-2

[2] K. Kulik-Kupka, J. Nowak, I. Korzonek-Szlacheta, B. Zubelewicz-Szkodzińska, The effects of endocrine disrupting chemicals on the human organism, Adv. Clin. Exp. Med. **71**, 1231-1238 (2017). https://doi.org/10.5604/01.3001.0010.7748

[3] M. Durante, J. Debus, J.S. Loeffler, Physics and biomedical challenges of cancer therapy with accelerated heavy ions. Nat. Rev. Phys. **3**, 777–790 (2021). https://doi.org/10.1038/s42254-021-00368-5

[4] E. Alizadeh, Th. M. Orlando, L. Sanche, Direct and Indirect Effects of Low-Energy Electrons on DNA, Annu. Rev. Phys. Chem. **66**, 379–98 (2015). https://doi.org/10.1146/annurev-physchem-040513-103605

[5] I. Friis, A.V. Verkhovtsev, I.A. Solov'yov, A.V. Solov'yov, Lethal DNA damage caused by ion-induced shock waves in cells, Phys. Rev. E **104**, 054408 (2021). https://doi.org/10.1103/PhysRevE.104.054408

[6] U. Amaldi, G. Kraft, Radiotherapy with Beams of Carbon Ions, Rep. Prog. Phys. **68**, 1861−1882 (2005). https://doi.org/10.1088/0034-4885/68/8/R04

[7] M. C. Fuss, A. Muñoz, J. C. Oller, F. Blanco, P. Limão-Vieira, A. Williart, C. Huerga, M. Téllez, G. García, Energy deposition model for I-125 photon radiation in water, Eur. Phys. J. D **60**, 203–208 (2010). https://doi.org/10.1140/epjd/e2010-00174-8

[8] M.C. Fuss, A.G. Sanz, A. Munoz, F. Blanco, M.J. Brunger, S.J. Buckman, P. Limao-Vieira, G. Garcıa, Current prospects on Low Energy Particle Track Simulation for Biomedical Applications, Appl. Radiat. Isot**.** **83**,159–164 (2014). http://dx.doi.org/10.1016/j.apradiso.2013.01.017

[9] L. Sanche, Beyond radical thinking, Nature **461**, 358–359 (2009). https://doi.org/10.1038/461358a

[10] B. Boudaıffa, P. Cloutier, D. Hunting, M.A. Huels, L. Sanche, Resonant formation of DNA strand breaks by low-energy (3 to 20 eV) electrons, Science **287**, 1658-1660 (2000). https://doi.org/10.1126/science.287.5458.1658

[11] I. Baccarelli, I. Bald, F.A. Gianturco, E. Illenberger, J. Kopyra, Electron-induced damage of DNA and its components: Experiments and theoretical models, Phys. Rep. **508,** 1–44 (2011). https://doi.org/10.1016/j.physrep.2011.06.004

[12] X. Pan and L. Sanche, Mechanism and Site of Attack for Direct Damage to DNA by Low-Energy Electrons, Phys. Rev. Lett. **94**, 198104 (2005). https://doi.org/10.1103/PhysRevLett.94.198104

[13] P. Sulzer, S. Ptasińska, F. Zappa, B. Mielewska, A. R. Milosavljevic, P. Scheier, T. D. Märk, I. Bald, S. Gohlke, M. A. Huels, E. Illenberger, Dissociative electron attachment to furan, tetrahydrofuran, and fructose, J. Chem. Phys. **125**, 044304 (2006). https://doi.org/10.1063/1.2222370

[14] S. Ptasińska, S. Denifl, V. Grill, T. D. Märk, E. Illenberger, P. Scheier, Bond- and Site-Selective Loss of H− from Pyrimidine Bases, Phys. Rev. Lett. **95**, 093201 (2005). https://doi.org/10.1103/PhysRevLett.95.093201

[15] T. J. Wasowicz, I. Linert, I. Lachowicz, M. Zubek, Electron impact fragmentation of pyrrole molecules studied by fluorescence emission spectroscopy. Photonics Lett. Pol. **3**, 110–112 (2011). https://doi.org/10.4302/plp.2011.3.07

[16] M. C. Fuss, L. Ellis-Gibbings, D. B. Jones, M. J. Brunger, F. Blanco, A. Muñoz, P. Limão-Vieira, G. García, The role of pyrimidine and water as underlying molecular constituents for describing radiation damage in living tissue: A comparative study, J. Appl. Phys. **117**, 214701 (2015). https://doi.org/10.1063/1.4921810

[17] J.A. Trocchi, J. Dech, W. Kedzierski, J. W. McConkey, Production of excited H–atoms in electron collisions with adenine, J. Phys. B At. Mol. Opt. Phys. **52**, 055204 (2019). https://doi.org/10.1088/1361-6455/ab0222

[18] Z. Li, I. Carmichael, S. Ptasinska, Dissociative electron attachment induced ring-opening in five-membered heterocyclic compounds, Phys. Chem. Chem. Phys. **20**, 18271-18278 (2018). https://doi.org/10.1039/C8CP02718H

[19] E. Nováková, L. Vyšín, T. Burian, L. Juha, M. Davídková, V. Múčka, V. Čuba, M. E. Grisham, S. Heinbuch, J. J. Rocca, Breaking DNA strands by extreme-ultraviolet laser pulses in vacuum, Phys. Rev. E **91**, 042718 (2015). https://doi.org/10.1103/PhysRevE.91.042718

[20] O. González-Magaña, M. Tiemens, G. Reitsma, L. Boschman, M. Door, S. Bari, P. O. Lahaie, J. R. Wagner, M. A. Huels, R. Hoekstra, and T. Schlathölter, Fragmentation of protonated oligonucleotides by energetic photons and C^{q+} ions, Phys. Rev. A **87**, 032702 (2013). https://doi.org/10.1103/PhysRevA.87.032702

[21] T.J. Wasowicz, A. Kivimäki, M. Dampc, M. Coreno, M. de Simone, M. Zubek, Photofragmentation of tetrahydrofuran molecules in the vacuum-ultraviolet region via superexcited states studied by fluorescence spectroscopy, Phys. Rev. A **83**, 033411 (2011). https://doi.org/10.1103/PhysRevA.83.033411

[22] G. Vall-llosera, M. Coreno, P. Erman, M. A. Huels, K. Jakubowska, A. Kivimäki, E. Rachlew, M. Stankiewicz, VUV photoionisation of free azabenzenes: Pyridine, pyrazine, pyrimidine, pyridazine and s-triazine, Int. J. Mass Spectrom. **275**, 55-63 (2008). https://doi.org/10.1016/j.ijms.2008.05.019

[23] T. J. Wasowicz, I. Dąbkowska, A. Kivimäki, R. Richter, Two-body dissociation of isoxazole following double photoionization – an experimental PEPIPICO and theoretical DFT and MP2 study, Phys. Chem. Chem. Phys. **00**, 00-00 (2023). https://doi.org/10.1039/D3CP03760F

[24] T. J. Wasowicz, I. Ljubić, A. Kivimäki, R. Richter, Core-shell excitation of isoxazole at the C, N, and O K-edges – an experimental NEXAFS and theoretical TD-DFT study, Phys. Chem. Chem. Phys. **24**, 19302-19313 (2022). https://doi.org/10.1039/D2CP02366K

[25] T. J. Wasowicz, A. Kivimäki, D. Catone, R. Richter, Vacuum Ultraviolet Photoionization and Ionic Fragmentation of the Isoxazole Molecules. Int. J. Mass Spectrom. **449**, 116276, (2020). https://doi.org/10.1016/j.ijms.2019.116276

[26] T. J. Wasowicz, I. Dąbkowska, A. Kivimäki, M. Coreno, M. Zubek, Elimination and migration of hydrogen in the vacuum-ultraviolet photodissociation of pyridine molecules. J. Phys. B Atom. Mol. Opt. Phys. **50**, 015101 (2017). https://doi.org/10.1088/1361-6455/50/1/015101

[27] T. J. Wasowicz, A. Kivimäki, M. Coreno, M. Zubek, Formation of CN ($B^2\Sigma^+$) radicals in the vacuum-ultraviolet photodissociation of pyridine and pyrimidine molecules, J. Phys. B: At. Mol. Opt. Phys. **47**, 055103 (2014). https://doi.org/10.1088/0953-4075/47/5/055103

[28] M. Zubek, T. J. Wasowicz, I. Dąbkowska, A. Kivimäki, M. Coreno, Hydrogen Migration in Formation of NH($A^3\Pi$) Radicals Via Superexcited States in Photodissociation of Isoxazole Molecules, J. Chem. Phys. **141**, 064301 (2014). https://doi.org/10.1063/1.4891808

[29] A. K. Dharmadhikari, H. Bharambe, J. A. Dharmadhikari, J. S. D'Souza, D. Mathur, DNA Damage by OH Radicals Produced Using Intense, Ultrashort, Long Wavelength Laser Pulses, Phys. Rev. Lett. **112**, 138105 (2014). https://doi.org/10.1103/PhysRevLett.112.138105

[30] J. de Vries, R. Hoekstra, R. Morgenstern, and T. Schlathölter, Charge Driven Fragmentation of Nucleobases, Phys. Rev. Lett. **91**, 053401 (2003). https://doi.org/10.1103/PhysRevLett.91.053401

[31] Z. Deng, I. Bald, E. Illenberger, M. A. Huels, Beyond the Bragg Peak: Hyperthermal Heavy Ion Damage to DNA Components, Phys. Rev. Lett. **95**, 153201 (2005). https://doi.org/10.1103/PhysRevLett.95.153201

[32] I. Bald, Z. Deng, E. Illenberger, M.A. Huels, 10–100 eV Ar+ ion induced damage to d-ribose and 2-deoxy-d-ribose molecules in condensed phase, Phys. Chem. Chem. Phys. **8**, 1215-1222 (2006). https://doi.org/10.1039/B514754A

[33] F. Alvarado, S. Bari, R. Hoekstra, T. Schlathöter, Quantification of Ion-Induced Molecular Fragmentation of Isolated 2-Deoxy-D-ribose Molecules, Phys. Chem. Chem. Phys. **8**, 1922−1928 (2006). https://doi.org/10.1039/B517109A

[34] J. Tabet, S. Eden, S. Feil, H. Abdoul-Carime, B. Farizon, M. Farizon, S. Ouaskit, T.D. Märk, Mass spectrometry (fragmentation ratios) of DNA base molecules following 80keV proton impact with separation of direct ionization and electron capture processes, Int. J. Mass Spectrom. **292**, 53-63, (2010). https://doi.org/10.1016/j.ijms.2010.03.002

[35] T. J. Wasowicz, B. Pranszke, Fragmentation of Tetrahydrofuran Molecules by H+, C+, and O+ Collisions at the Incident Energy Range of 25–1000 eV, J. Phys. Chem. A **119**, 581–589 (2015). https://doi.org/10.1021/jp5105856

[36] S. Maclot, R. Delaunay, D. G. Piekarski, A. Domaracka, B. A. Huber, L. Adoui, F. Martín, M. Alcamí, L. Avaldi, P. Bolognesi, S. Díaz-Tendero, and P. Rousseau, Determination of Energy-Transfer Distributions in Ionizing Ion-Molecule Collisions, Phys. Rev. Lett. **117**, 073201 (2016). https://doi.org/10.1103/PhysRevLett.117.073201

[37] T. J. Wasowicz, B. Pranszke, Observation of the Hydrogen Migration in the Cation-Induced Fragmentation of the Pyridine Molecules. J. Phys. Chem. A **120**, 964-971, (2016). https://doi.org/10.1021/acs.jpca.5b11298

[38] T. J. Wasowicz, B. Pranszke, Interactions of protons with furan molecules studied by collision-induced emission spectroscopy at the incident energy range of 50–1000 eV. Eur. Phys. J. D **70**, 175 (2016). https://doi.org/10.1140/epjd/e2016-70308-1

[39] C. Covington, K. Hartig, A. Russakoff, R. Kulpins, K. Varga, Time-dependent density-functional-theory investigation of the collisions of protons and α particles with uracil and adenine, Phys. Rev. A **95**, 052701 (2017). https://doi.org/10.1103/PhysRevA.95.052701

[40] T. J. Wasowicz, M. Łabuda, B. Pranszke, Charge Transfer, Complexes Formation and Furan Fragmentation Induced by Collisions with Low-Energy Helium Cations. Int. J. Mol. Sci. **20**, 6022 (2019). https://doi.org/10.3390/ijms20236022

[41] C. Mejía, G.S. Vignoli Muniz, M. Bender, D. Severin, C. Trautmann, B. Augé, A.N. Agnihotri, P. Boduch, A. Domaracka, H. Rothard, Swift heavy ion irradiation of thymine at cryogenic temperature, Nucl. Instrum. Methods Phys. Res. B **534**, 11-15 (2023). https://doi.org/10.1016/j.nimb.2022.10.024

[42] D.T. Debela, S.G.Y. Muzazu, K.D. Heraro, M.T. Ndalama, B.W. Mesele, D.C. Haile, S.K. Kitui, T. Manyazewal, New approaches and procedures for cancer treatment: Current perspectives, SAGE Open Med. **9**, 20503121211034366 (2021). https://doi.org/10.1177/20503121211034366

[43] P. Wachsberger, R. Burd, A.P. Dicker, Tumor Response to Ionizing Radiation Combined with Antiangiogenesis or Vascular Targeting Agents: Exploring Mechanisms of Interaction, Clin. Cancer Res. **9**, 1957–1971 (2003).

[44] L. Pihlava, M. Berholts, J. Niskanen, A. Vladyka, K. Kooser, C. Stråhlman, P. Eng-Johnsson, A. Kivimäki and E. Kukk, Photodissociation of bromine-substituted nitroimidazole radiosensitizers, Phys. Chem. Chem. Phys. **25**, 13004–13011 (2023) https://doi.org/10.1039/D2CP04888D

[45] L. Gong, Y. Zhang, C. Liu, M. Zhang, and S. Han, Application of Radiosensitizers in Cancer Radiotherapy, Int. J. Nanomed. **16**, 1083 (2021). https://doi.org/10.2147/IJN.S290438

[46] G. L. Beretta, F. Zunino, Molecular Mechanisms of Anthracycline Activity, Top. Curr. Chem. **283**, 1–19 (2008). https://doi.org/10.1007/128_2007_3

[47] P.W. Smith, S.L. Sollis, P.D. Howes, P.C. Cherry, I.D. Starkey et al., Dihydropyrancarboxamides Related to Zanamivir: A New Series of Inhibitors of Influenza Virus Sialidases. 1. Discovery, Synthesis, Biological Activity, and Structure-Activity Relationships of 4-Guanidino- and 4-Amino-4H-pyran-6-carboxamides, J. Med. Chem. **41**, 787-797 (1998). https://doi.org/10.1021/jm970374b

[48] J. Kaplan, J.C. Verheijen, N. Brooijmans, L. Toral-Barza, I. Hollander, K. Yu, A. Zask, Discovery of 3,6-dihydro-2H-pyran as a morpholine replacement in 6-aryl-1H-pyrazolo[3,4-d]pyrimidines and 2-arylthieno[3,2-d]pyrimidines: ATP-competitive inhibitors of the mammalian target of rapamycin (mTOR), Bioorg. Med. Chem. Lett. **20**, 640–643 (2010). https://doi.org/10.1016/j.bmcl.2009.11.050

[49] H.Y. Zhou, F.Q. Dong, X.L. Du, Z.K. Zhou, H.R. Huo et al., Antitumor activities of biscoumarin and dihydropyran derivatives, Bioorg. Med. Chem. Lett. **26**, 3876-3880 (2016). https://doi.org/10.1016/j.bmcl.2016.07.023

[50] C. Musial, A. Kuban-Jankowska, M. Gorska-Ponikowska, Beneficial Properties of Green Tea Catechins. Int. J. Mol. Sci. **21**, 1744 (2020). https://doi.org/10.3390/ijms21051744

[51] L.-S. Tran, O. Herbinet, H.-H. Carstensen, F. Battin-Leclerc, Chemical kinetics of cyclic ethers in combustion, Prog. Energy Combust. Sci. **92**, 101019 (2022). https://doi.org/10.1016/j.pecs.2022.101019

[52] A. L. Koritzke, K. M. Frandsen, M. G. Christianson, J. C. Davis, A. C. Doner, et al., Fragmentation mechanisms from electron-impact of complex cyclic ethers formed in combustion, Int. J. Mass Spectrom. **454**, 116342 (2020). https://doi.org/10.1016/j.ijms.2020.116342

[53] M. Dampc, E. Szymańska, B. Mielewska, M. Zubek, Ionization and ionic fragmentation of tetrahydrofuran molecules by electron collisions, J. Phys. B: At. Mol. Opt. Phys. **44**, 55206 (2011). https://doi.org/10.1088/0953-4075/44/5/055206

[54] M. K. Jurkowski, T. J. Wasowicz, Dehydrogenation in electron-induced dissociative ionization of pyridine molecule, Rom. J. Phys. **68**, 205 (2023). https://doi.org/10.59277/RomJPhys.2023.68.205

[55] M. Dampc, P. Możejko, M. Zubek, Electron impact ionization and cationic fragmentation of the pyridazine molecules. Eur. Phys. J. D **72**, 216 (2018). https://doi.org/10.1140/epjd/e2018-90474-2

[56] P.J. Linstrom and W.G. Mallard, Eds., NIST Chemistry WebBook, NIST Standard Reference Database Number 69, National Institute of Standards and Technology, Gaithersburg MD, 20899, https://doi.org/10.18434/T4D303 (retrieved December 15, 2023).

[57] 3,4-Dihydro-2H-pyran. Available online: https://www.sigmaaldrich.com/PL/pl/substance/34dihydro2hpyran8412110872 (accessed on November 3, 2023).

[58] 3,4-Dihydro-2H-pyran. http://www.chemspider.com/Chemical-Structure.7789.html (accessed on November 3, 2023).

[59] S. Grimme, Towards First Principles Calculation of Electron Impact Mass Spectra of Molecules, Angew. Chem. Int. Ed. **52**, 6306-6312 (2013). https://doi.org/10.1002/anie.201300158

[60] C. A. Bauer, S. Grimme, How to Compute Electron Ionization Mass Spectra from First Principles, J. Phys. Chem. A **120**, 3755-3766 (2016). https://doi.org/10.1021/acs.jpca.6b02907

[61] S. Grimme, C. Bannwarth, P. Shushkov, A Robust and Accurate Tight-Binding Quantum Chemical Method for Structures, Vibrational Frequencies, and Noncovalent Interactions of Large Molecular Systems Parametrized for All spd-Block Elements (Z = 1–86), J. Chem. Theory Comput. **13**, 1989-2009 (2017). https://doi.org/10.1021/acs.jctc.7b00118

[62] J. Koopman, S. Grimme, Calculation of Electron Ionization Mass Spectra with Semiempirical GFNn-xTB Methods, ACS Omega **4**, 15120-15133 (2019). https://doi.org/10.1021/acsomega.9b02011

[63] C. Adamo, V. Barone, Toward reliable density functional methods without adjustable parameters: The PBE0 model, J. Chem. Phys. **110**, 6158-6169 (1999). https://doi.org/10.1063/1.478522

[64] F. Weigend, R. Ahlrichs, Balanced basis sets of split valence, triple zeta valence and quadruple zeta valence quality for H to Rn: Design and assessment of accuracy, Phys. Chem. Chem. Phys. **7**, 3297-3305 (2005). https://doi.org/10.1039/B508541A

[65] E. Caldeweyher, S. Ehlert, A. Hansen, H. Neugebauer, S. Spicher, C. Bannwarth, S. Grimme, A generally applicable atomic-charge dependent London dispersion correction, J. Chem. Phys. **150**, 154122 (2019). https://doi.org/10.1063/1.5090222

[66] F. Neese, The ORCA program system, WIREs: Comp. Mol. Sci. **2**, 73-78, (2012). https://doi.org/10.1002/wcms.81

[67] F. Neese, Software update: The ORCA program system—Version 5.0, WIREs: Comp. Mol. Sci. **12**, e1606, (2022). https://doi.org/10.1002/wcms.1606

[68] A. L. Harris, J. Nepomuceno, A Data-Driven Machine Learning Approach for Electron-Molecule Ionization Cross Sections, J. Phys. B: At. Mol. Opt. Phys. **57** 025201 (2024) https://doi.org/10.1088/1361-6455/ad2185

[69] M. Jurkowski, T. J. Wasowicz, (2021, June 14-18) *Ionization and fragmentation of the six-membered heterocycles containing oxygen – comparative studies on electron and photon impact on the 3,4-dihydro-2H-pyran molecules*. The 9th International Conference on Radiation in Various Fields of Research, Herceg Novi, Montenegro https://doi.org/10.21175/rad.abstr.book.2021.30.3

[70] S. Wang, T. Kind, D. J. Tantillo, O. Fiehn, Predicting in silico electron ionization mass spectra using quantum chemistry, J. Cheminform. **12**, 63 (2020). https://doi.org/10.1186/s13321-020-00470-3

[71] S. Wang, T. Kind, P. L. Bremer, D. J. Tantillo, O. Fiehn, Quantum Chemical Prediction of Electron Ionization Mass Spectra of Trimethylsilylated Metabolites, Anal. Chem. **94**, 1559-1566 (2022). https://doi.org/10.1021/acs.analchem.1c02838

[72] C. Bannwarth, S. Ehlert, S. Grimme, GFN2-xTB—An Accurate and Broadly Parametrized Self-Consistent Tight-Binding Quantum Chemical Method with Multipole Electrostatics and Density-Dependent Dispersion Contributions, J. Chem. Theory Comput. **15**, 1652-1671 (2019). https://doi.org/10.1021/acs.jctc.8b01176

[73] M. H. Stockett, H. Zettergren, L. Adoui, J. D. Alexander, U. Bērziņš, T. Chen, M. Gatchell, N. Haag, B. A. Huber, P. Hvelplund, A. Johansson, H. A. B. Johansson, K. Kulyk, S. Rosén, P. Rousseau, K. Støchkel, H. T. Schmidt, and H. Cederquist, Non-statistical fragmentation of large molecules, Phys. Rev. A **89**, 032701 (2014), https://doi.org/10.1103/PhysRevA.89.032701

[74] M. Gatchell, M.H. Stockett, P. Rousseau, T. Chen, K. Kulyk, H.T. Schmidt, J.Y. Chesnel, A. Domaracka, A. Méry, S. Maclot, L. Adoui, K. Støchkel, P. Hvelplund, Y. Wang, M. Alcamí, B.A. Huber, F. Martín, H. Zettergren, H. Cederquist, Non-statistical fragmentation of

PAHs and fullerenes in collisions with atoms, Int. J. Mass Spectrom., **365–366**, 260 (2014), https://doi.org/10.1016/j.ijms.2013.12.013

[75] S. Rashid, A. Sit, B. West, P.M. Mayer, Colliding the hydrocarbon building blocks of astrochemical polycyclic aromatic hydrocarbons with 8 keV He^+ and H_2^+ ions: Luminescence from methane, acetylene, benzene and naphthalene, Chem. Phys. Lett. **667**, 129-136 (2017), https://doi.org/10.1016/j.cplett.2016.11.052

[76] T. J. Wasowicz, Formation of OH radicals as evidence of intramolecular hydrogen migration in cation-induced dissociation of furan molecules, Rom. J. Phys. **67**, 206 (2022)

[77] P. J. Stephens, F. J. Devlin, C. F. Chabalowski, M. J. Frisch, Ab Initio Calculation of Vibrational Absorption and Circular Dichroism Spectra Using Density Functional Force Fields, J. Phys. Chem. **98**, 11623-11627 (1994). https://doi.org/10.1021/j100096a001

[78] Y. Zhao, D. G. Truhlar, The M06 suite of density functionals for main group thermochemistry, thermochemical kinetics, noncovalent interactions, excited states, and transition elements: two new functionals and systematic testing of four M06-class functionals and 12 other functionals, Theor. Chem. Acc. **120**, 215-241 (2008). https://doi.org/10.1007/s00214-007-0310-x

[79] T. Yanai, D. Tew, N. Handy, A new hybrid exchange-correlation functional using the Coulomb-attenuating method (CAM-B3LYP), Chem. Phys. Lett. **393**, 51-57 (2004). https://doi.org/10.1016/j.cplett.2004.06.011

[80] M. A. Rahman, E. Krishnakumar, Communication: Electron ionization of DNA bases, J. Chem. Phys. **144**, 161102 (2016). https://doi.org/10.1063/1.4948412

[81] R. Rejoub, B. G. Lindsay, R. F. Stebbings, Determination of the absolute partial and total cross sections for electron-impact ionization of the rare gases, Phys. Rev. A **65**, 042713 (2002). https://doi.org/10.1103/PhysRevA.65.042713

[82] D. Hein H. Al-Khazraji, C. J. Tiessen, D. Lukic, J. A. Trocchi, J. W. McConkey, Excited atomic fragments following electron dissociation of pyrimidine, J. Phys. B: At. Mol. Opt. Phys. **46,** 045202 (2013). https://doi.org/10.1088/0953-4075/46/4/045202

[83] C.Q. Jiao, J.C.A. DeJoseph, R. Lee, A. Garscadden, Kinetics of electron impact ionization and ion-molecule reactions of pyridine, Int. J. Mass Spectrom. **257**, 34–40 (2006), https://doi.org/10.1016/j.ijms.2006.06.007

[84] I. Linert, M. Dampc, B. Mielewska, M. Zubek, Cross sections for ionization and ionic fragmentation of pyrimidine molecules by electron collisions, Eur. Phys. J. D **66**, 20 (2012) https://doi.org/10.1140/epjd/e2011-20648-3

[85] G. H. Wannier, The Threshold Law for Single Ionization of Atoms or Ions by Electrons, Phys. Rev. **90**, 817 (1953), https://doi.org/10.1103/PhysRev.90.817

[86] M. K. Jurkowski, D. Glowienka, T. J. Wasowicz, ThreSpect − a Program for the Determination of the Appearance Energies of Neutral and Ionized Species, Rom. J. Phys. **68**, 203 (2023).

[87] M. Jurkowski, D. Glowienka, T. Wasowicz, *ThreSpect a program for the determination of the Appearance Energies* [Data set]. Gdansk University of Technology (2023), https://doi.org/10.34808/hwc6-be20

[88] M. Bloch, F. Brogli, E. Heilbronner, T.B. Jones, H. Prinzbach, O. Schweikert, Photoelectron spectra of unsaturated oxides. I. 1,4-dioxin and related systems, Helv. Chim. Acta **61**, 1388-1398 (1978), https://doi.org/10.1002/hlca.19780610422

[89] K. Watanabe, T. Nakayama, J. Mottl, Ionization potentials of some molecules, J. Quant. Spectrosc. Radiat. Transf. **2**, 369-382 (1962), https://doi.org/10.1016/0022-4073(62)90023-7

[90] A.A. Planckaert, J. Doucet, C. Sandorfy, Comparative study of the vacuum ultraviolet absorption and photoelectron spectra of some simple ethers and thioethers, J. Chem. Phys. **60**, 4846-4853 (1974), https://doi.org/10.1063/1.1680992

[91] C. Batich, E. Heilbronner, C.B. Quinn, J.R. Wiseman, The electronic structure of vinyl ethers and sulfides with interrupted conjugation examined by photoelectron spectroscopy, Helv. Chim. Acta **59**, 512-522 (1976), https://doi.org/10.1002/hlca.19760590217

[92] S. SenGupta; H. P. Upadhyaya; A. Kumar; P. D. Naik; P. Bajaj, Detection of OH radical in laser induced photodissociation of tetrahydrofuran at 193 nm, J. Chem. Phys. **122**, 124309 (2005), https://doi.org/10.1063/1.1867354

[93] R. Taylor, The mechanism of thermal eliminations. Part 25. Arrhenius data for pyrolysis of isochroman-3-one, benzyl methyl ether, 2-hydroxyethylbenzene, phenyl acetate, and 3,4-dihydro-2H-pyran, J. Chem. Soc., Perkin Trans. 2, No.2, 183-189 (1988), https://doi.org/10.1039/P29880000183

[94] C. A. Wellington, Gas-phase pyrolysis of 3,4-dihydro-2H-pyran, J. Chem. Soc. A, Iss. 0, 2584 (1969), https://doi.org/10.1039/J19690002584

[95] L. Zeng, S. Liu, Y. Lan, L. Gao, Catalytic asymmetric oxa-Diels–Alder reaction of acroleins with simple alkenes, Nat. Commun. **14**, 3511 (2023), https://doi.org/10.1038/s41467-023-39184-z